Programmed nanocloak of commensal bacteria-derived nanovesicles amplify strong immunoreactivity against tumor growth and metastatic progression

Jingjing Zhang[1#], Shuangshuang Wan[1#], Hao Zhou[2#], Jiaxin Du[1], Yaocheng Li[1], Houjuan Zhu[3], Lixing Weng[1], Xianguang Ding[1], Lianhui Wang[1*]*

[1]State Key Laboratory of Organic Electronics and Information Displays & Jiangsu Key Laboratory for Biosensors, Institute of Advanced Materials (IAM), Nanjing University of Posts and Telecommunications, Nanjing 210023, China

[2]Department of General Surgery, The First Affiliated Hospital of Soochow University, Suzhou, Jiangsu Province, China

[3]A*STAR (Agency for Science, Technology and Research), Singapore 138634, Singapore

[#]These authors contributed equally

Email: iamxgding@njupt.edu.cn (XGD); iamlhwang@njupt.edu.cn (LHW)

ABSTRACT

Intratumoral bacteria hold great promise as novel molecular targets of tumors to improve cancer treatment. However, direct leveraging in vivo antibacterial strategies such as antibiotics for cancer therapy often leads to uncertain effectiveness, mainly due to poor selectivity together with potential adverse effects. Here, building from the clinical discovery that patients with breast cancer featured rich commensal bacteria, we developed an activatable biointerface by encapsulating commensal bacteria-derived extracellular vesicles (BEV) with responsive nanocloak to potentiate immunoreactivity against intratumoral bacteria and breast cancer. We show the interfacially cloaked BEV (cBEV) not only overcame serious systemic side responses but also demonstrated heightened immunogenicity by responsive exposure immunogenicity intercellularly, facilitating DCs maturation through activating the STING pathway. As a preventive measure, vaccination with nanocloaked cBEVs achieved strong protection against bacterial infection, largely providing prophylactic efficiency against tumor challenges. When combined with anti-PD-L1 antibodies, this approach elicited a potent tumor-specific immune response, synergistically inhibiting tumor progression and mitigating lung metastases.

KEYWORDS: *Extracellular vesicle, Nano-biointerface, cGAS-STING pathway, Cancer immunotherapy, Intratumoral bacteria*

TEXT

Introduction

Bacterial infections are closely correlated with multiple types of cancers, contributing to more than 16% of global cancer incidence.[1,2] Clinical observations have identified the presence of bacteria across diverse tumor types,[3,4] exerting a notable influence on cancer progression.[5,6] Accumulating evidence demonstrated that modulating the microbiome can yield discernible effects on the outcomes of cancer treatment.[7,8] Therefore, intratumor bacteria emerge as an attractive molecular target of tumor intervention,[9] offering an alternative avenue for early cancer prevention and more efficacious treatment strategies. While the relationship between intratumor bacteria and cancer is being increasingly understood, developing microbiota therapeutics specifically designed to target certain types of tumor bacteria presents significant challenges.[10] It is crucial to differentiate between beneficial and harmful bacteria within certain types of cancer, as some bacteria may play a protective role against cancer.[11] Additionally, the task of creating effective antibacterial strategies that are both safe and specific to intratumor bacteria is intricate. Although current well-established antibiotics are effective against a broad spectrum of bacteria, the emergence of antibiotic resistance raises serious concerns.[12,13] Furthermore, the use of broad-spectrum antibiotics poses a threat to microbiome diversity, potentially compromising the effectiveness of cancer treatments such as immunotherapy. As a result, developing precisely targeted therapeutics directed to intratumoral bacteria is highly desirable for the prevention and treatment of specific types of cancer.

Antibacterial vaccines offer an attractive approach to cost-effective and precise intervention against intratumor bacteria.[14] Working by stimulating the immune system, the vaccine can boost

the immune response to produce antibodies and activated immune cells that recognize and combat specific bacteria or groups of closely related bacteria.[15,16] Compared with antibiotics, antibacterial vaccines show distinct advantages of precision and long-lasting protective effects. While the overuse and misuse of antibiotics often lead to the rise of antibiotic-resistant bacteria, antibacterial vaccines do not encounter issues related to resistance.[17] Despite recent progress, the development of efficacious and safe vaccines is challenging. Antibacterial vaccines employing attenuated bacteria,[18,19,20] while highly immunogenic, raise potential safety concerns, especially for individuals with compromised immune systems. On the other hand, inactivated bacterial vaccines are generally perceived as safer,[21,22] yet they often fall short in terms of eliciting robust protective immunity against bacteria due to insufficient immunogenicity. Bacterial vaccines utilizing inactivated subunit antigens or toxoids also encounter challenges related to suboptimal antigenicity.[23] Addressing these challenges for in vivo applications necessitates the development of novel bacterial vaccine strategies.

Herein, we demonstrated that *Bacteroides fragilis* (*B. fragilis*) was abundantly colonized in breast cancer with a strong positive correlation to breast tumor growth and metastasis. We then employed *B. fragilis*-derived extracellular vesicles (BEVs) and leveraged a "nanocloak" strategy utilizing highly biocompatible manganese oxide (MnO_2) to program the immunointerface of BEVs to achieve nanocloaked BEV (cBEV) with pH-responsive behavior. Upon internalization by DCs, the lysosome-triggered dissolution of nanocloaked BEV resulted in the release of Mn^{2+} and accelerated activation of DC cells, resulting in significant inhibition of bacterial growth within tumors. Furthermore, we assessed the prophylactic potential of cBEV and its synergistic therapeutic effects when combined with anti-PD-L1 treatment against breast cancer. The pre-

immunization with cBEV could largely protect healthy mice from MCF-7 tumor challenge by preventing *B. fragilis* infections. Moreover, in *B. fragilis*-infected breast tumor models, cBEV nanovaccines effectively inhibited tumor commensal bacteria in the primary tumor and lung metastases by synergizing the therapeutic efficacy of anti-PD-L1 treatment.

Results

Bacteroides fragilis commensalism in patients with breast cancer

We started by collecting clinical samples from patients with breast cancer, including both cancerous and benign tissues, and then analyzed the microbes present in these samples using 16S rRNA sequencing. The Venn diagrams in Figure 1a indicated that cancerous samples had more unique operational taxonomic units (OTUs). Additionally, the microbial communities in cancerous and non-cancerous tissues differed distinctly based on the principal coordinate analysis (PCoA) using Bray-Curtis distance (Figure 1b, $p = 0.044$). Moreover, the microbial α diversity index (including Chao1 diversity index, observed species and Shannon diversity index) in cancerous tissues was found to be significantly higher when compared to the non-cancerous group (Figure 1c). The results above demonstrated the different profiles of microbes in cancerous and benign tissues and implied that the canceration of the tissue may be associated with different compositions and abundance of the tumoral colonized microbes. To further explore the altered bacterial species, the expression of bacteria at the genus level from different tissue samples was analyzed, of which *Bacterodies* and *Oscillospira* were found to exhibit a remarkable contrast compared to other bacteria (Figure 1d and Figure S1), consistent with previous meta-analysis on clinical breast cancer data. To further investigate whether these tumoral bacterial matter to breast cancer, two different bacteria, *Bacteroides fragilis* (*B. fragilis*) and *Oscillospira guilliermondii*

(*O.guilliermondii*) were chosen to be intratumorally injected into MCF-7 tumor-bearing mice separately three times (Figure 1e). It was found that among different treatments, *B. fragilis* induced the most significant tumor growth and metastasis (Figure. 1f,g and Figure S2), which was further confirmed by hematoxylin & eosin (H&E) staining of lung tissues (Figure 1h). These data not only confirmed the high abundance of *B. fragilis* present in breast tumors but also revealed their significant role in breast cancer progression, thus highlighting the opportunity of developing *B. fragilis*-targeting therapeutics for the prevention and treatment of breast cancer.

Immunocompetent antibacterial vaccines inhibit the progress of breast tumors

Given the strongly positive correlation between *B. fragilis* and breast tumors, we next explored whether breast tumors can be largely prevented by providing antibacterial vaccines against *B. fragilis* before oncogenesis. Antibacterial vaccination has been shown to be an effective strategy for fighting against specific bacterial colonization in tissue.[14,15] We initially evaluated the prophylactic effects of denatured *B. fragilis* (d-*B. fragilis*) and *B. fragilis*-derived EVs (BEVs), which were reported to inherit similar immunogenicity of their derives and capable of training host immunity,[24,25] on MCF-7 tumor model before challenged with the tumor cell and *B. fragilis* (Figure S3a). As a comparison, commonly used antibacterial agent, antibiotics, was employed as a control and consistently administered throughout the entire experiment. The in vivo imaging showed that while both d-*B. fragilis* and antibiotics showed certain effects on retarding tumor growth, *B. fragilis*-derived EVs achieved a more potent inhibition of tumor proliferation (Figure S3b-g). The relatively low tumor inhibition capacity of d-*B. fragilis* may be due to the loss of immunogenicity during the denature process thus insufficient immunoreactivity against antibacterials.[21,22] The calculated tumor growth inhibition (TGI) response of BEV was up to 49%,

compared to 17% for d-*B. fragilis* and 28% for antibiotics (Figure S3h). These results demonstrated that BEVs prepared from *B. fragilis* conferred more significant inhibitory effects against tumor growth.

However, in the course of our in vivo toxicity assessment, we identified serious systemic inflammatory responses. The serum levels of IFN-γ, TNF-α, and IL-6 in the BEV group dramatically increased by 5.86-, 3.99-, and 4.47-fold respectively, compared with that of the untreated group (Figure S4a). Furthermore, it was also observed that the mice exhibited poor tolerance to the BEV treatment, with body weight consistently lost obviously during treatment (Figure S4b). This natural bacterial EV-raised toxicity has also been observed in previous studies,[26] presumably attributable to the endotoxin exposure. This highlights the need to develop alternative means of BEV therapeutics to improve *B. fragilis*-target therapy.

Design and synthesis of nanocloaked cBEVs

To achieve mitigated toxicity and improved vaccination, we designed an artificial exoskeleton encapsulating the surface of BEV to form cloaked BEVs (cBEV). To produce cBEV, *B. fragilis*-derived EVs (BEV) were first collected. Subsequently, manganese dioxide (MnO_2), a commonly used biocompatible nanomaterial known for its pH-responsive characteristics,[27,28] was employed to construct the coating on BEVs. This process was accomplished through a mild and in-situ biomineralization route conducted on a microfluidic chip (Figure 2a and 2b), potentiating the bench-to-clinic translation with scalable production. In comparison to native BEVs, which show a typical cup-like vesicular structure under negative staining, the generated cBEV can be directly observed under the transmission electron microscope (TEM) and scanning electron microscope (SEM) without additional sample pre-treatment (Figure 2c and Figure S5a), which can be due to

the presence of high contrastive metal ions. The enlarged hydrodynamic diameter of the particle change up to around 142 nm supported the successful fabrication of the encapsulated nanostructure (cBEV) (Figure S5b). As a result of cloaking, the zeta potential of cBEV was slightly less negative than that of free BEVs (Figure S5c). The interface-mediated in situ nanocloaking reaction at mild aqueous conditions. Sodium dodecyl sulfate-polyacrylamide gel electrophoresis (SDS-PAGE) analysis confirmed that the protein of native BEVs largely remained after the degradation of cBEV, suggesting that the biomineralization process did not impair BEV integrity (Figure S5d). To further confirm the composition of cBEV, elemental mapping of the nanoparticles was carried out using energy-dispersive X-ray spectroscopy (EDX) (Figure 2d). The particles mainly contained three elements, which can be assigned to BEV (N, O) and MnO_2 (Mn, O). Additionally, the conventional characterization methods, such as X-ray photoelectron spectroscopy (XPS), also confirmed the nanocloaked layer formed (Figure S5e). This mild encapsulation process helps maintain the stability of BEVs by providing exoskeletons to protect BEVs against external stressors like temperature. Even after being cryopreserved at 4 ℃ and -80 ℃ for 30 days, there was no significant change in bioactivity, demonstrating the structural and biofunctional stability of the vesicles in the conventional laboratory storage environment (Figure 2e). This allows them to be stored and transported without compromising their efficacy, which is very crucial for BEV usage as vaccines in practical use.

With the prepared nanocloaked architecture, we evaluated the toxicity of nanocloaked BEVs. It was found that the cBEV caused minimal toxicity to HUVEC and DCs until the doses of 200 g mL^{-1} (Figure S6a). Meanwhile, in a wide range of cBEV concentrations tested, less than 5% of hemolysis was observed (Figure S6b). We further assessed whether the MnO_2 shells could efficiently shield BEVs from in vivo toxicity. Under the optimized concentrations, the spleen,

liver tissues, and other organs in cBEVs-treated mice through H&E staining revealed no apparent inflammatory cell infiltration (Figure 2f and Figure S7). Since systemic cytokine release is a common side effect associated with many immune agonists, we evaluated the in vivo toxicity of both cBEV and naked BEVs. In contrast to the BEVs, the cBEV group exhibited a significant reduction in serum levels of IL-6, TNF-α, and IFN-γ, with decreases of 38.0%, 37.6%, and 44.8%, respectively (Figure 2g). It was noted that the spleen weight in the cBEV group showed a significant decrease compared to the BEV group (Figure 2h). Moreover, the serum biochemical indexes remained within the normal range within 48 hours after subcutaneous injection of cBEV (Figure 2i and Figure S8). These findings suggest that cBEV exhibits enhanced biocompatibility, positioning it as a promising candidate for in vivo vaccine applications.

Collectively, our direct comparison of inflammatory responses revealed a substantial reduction in the toxicity of BEVs when employing manganese dioxide nanoarchitecture as a shielding agent. Additionally, an elevated degree of composite bacterial cBEV accumulation within lymph nodes was observed 24 hours post-injection (Figure 2j). This outcome is likely attributed to the protective influence exerted by manganese dioxide shells, which envelop the antigenic epitopes of the vesicles, thereby mitigating tissue clearance.[29] This heightened antigen accumulation in lymph nodes suggests a potential advantage for promoting adaptive immune activation.

cBEV promotes DCs maturation by activating STING pathway

Utilizing the well-established cBEV nanoarchitecture, we next evaluated their interaction with antigen-presenting cells (APCs), particularly dendritic cells (DCs), which serve as the primary APCs responsible for initiating adaptive immune responses.[30-32] Bone marrow-derived dendritic

cells (BMDCs) were first treated with cBEV in vitro for 24 hours and then specifically stained for CD11c (a marker of DCs), CD80, and CD86 (stimulatory markers of matured DCs). As shown by flow cytometry, cBEV treatment led to a significant increase in CD86 and CD80 expression on DCs, when compared to native BEVs (Figure 3a). Quantitative analysis suggested that the cBEV group resulted in 46.2% matured DCs, which was significantly higher (2.9-, 2.2-, and 1.8-fold) than the percentage observed in control (16.0%), BEV (21.3%), and MnO_2 group (25.6%) (Figure 3b), suggesting the capability of cBEV in potentiate DC maturation.

To further explore the mechanism of enhanced immunological activation, we investigated the classic DCs activation signaling pathways. Recent studies have identified that the presence of intracellular manganese ions may enhance the sensitivity of cGAS to cytosolic dsDNA, thereby amplifying the activation of the cGAS-STING pathway and triggering the production of type I IFN.[33-35] This, in turn, could facilitate the maturation of DCs (Figure 3c). We then examined the susceptibility of cBEVs under different exposure phases, spanning from prior to phagocytosis through to phagocytosis with lysosomal degradation, and culminating in DC maturation as a result of full exposure to the antigenic materials inside the DC cytoplasm. We first tested the pH responsiveness of the as-prepared cBEV under different exposure conditions by free manganese ions quantification. While cBEV showed no discernible changes at pH 7.4 and exhibited slight degradation under pH 6.5 conditions, which stimulate the pH of tumor microenvironment, the degradation process was rapidly initiated when the solution's pH reached 5, mimicking lysosomal conditions (Figure 3d). This indicates that cBEV was highly sensitive to the lysosomal conditions and quickly degraded to produce free manganese ions. The dissolution process was further confirmed by monitoring hydrodynamic size. The size of the cBEV nanoparticles decreased from 140 nm to around 100 nm, which was similar to the naked BEVs (Figure 3e).

These results imply that the MnO_2 nanoshell was more sensitive to the lysosomal mimicking condition. We therefore hypothesized that cBEV might decompose and release free manganese ions after internalization by DCs, resulting in Mn^{2+}-mediated STING pathway activation and resultant DCs maturation. We then evaluated the internalization of cBEV by DCs and the following intracellular exposure of manganese ions. After 4 hours of co-incubation with DCs, the DiD-labeled BEVs were localized within lysosomal structures (Figure 3f,g and Figure S9), indicating that cBEV had been internalized into BMDCs. The intracellular decomposition of cBEV was further assessed by quantifying intracellular free manganese ions with ICP-MS (Figure 3h). Following cBEV treatment, a notable presence of manganese ions was identified at the intracellular level. We then evaluated the activation of the intracellular STING pathway in response to cBEV treatment (Figure 3i). The immunofluorescence staining analysis showed that the expression of STING pathway-related proteins including phosphorylated STING (P-STING) and phosphorylated IRF3 (P-IRF3) in BMDCs was both increased after cBEV treatment, demonstrating the successfully intracellular activation of the STING pathway (Figure S10a, S10d). Consistently, The P-STING and P-IRF3 were also detected by flow cytometry after treatment with PBS, BEV, MnO_2 and cBEV (Figure S10b, S10e). The relative mean fluorescence intensities (MFIs) of P-STING and P-IRF3 from cBEV-internalized BMDC cells were approximately 7.7-, and 4.8-fold higher than those of the groups without treatment (Figure S10c, S10f). Furthermore, substantial IL-6, IFN-β and CXCL10 release were observed in cBEV-treated BMDCs compared to the BEV or MnO_2 treatment alone (Figure 3j). These results collectedly suggest the capability of MnO_2-nanocloaked BEVs in promoting DCs maturation. It is noteworthy that while MnO_2 treatment alone could activate the STING pathway, the direct intravenous administration of free Mn^{2+} may result in toxicity and rapid metabolism with

reduced tumor enrichment.[36] Meanwhile, the upregulated expression of IFN-β and CXCL10 in cBEV-treated DCs, indicated the activation of the STING pathway (Figure 3j), which could promote DC maturation. Collectively, these results indicated that cBEV could effectively activate the STING pathway and upregulate the IFN-β secretion, contributing to DC maturation.

Prophylactic efficiency of cBEV

We next evaluated the induction of humoral immunity in vivo after subcutaneous (s.c.) immunization with cBEV at an interval of 7 d (Figure 4a). We found the serum in the BEV and cBEV-treated group contained markedly higher (12.8-fold) immunoglobulin IgG antibody titers than samples from PBS, or MnO_2-treated mice after immunizations (Figure 4b). Meanwhile, the strong percentage of B cells ($CD19^+$) was observed in the cBEV group, which was 1.4-, 1.0- and 2.0-fold higher than that in the PBS, BEV and MnO_2 group, respectively, indicating a high portion of B cells in the lymph nodes (Figure 4c and Figure S11). When the serum from cBEV-vaccinated mice was incubated with *B. fragilis*, obviously bactericidal activity was observed (Figure 4d). After confirming the successful antibody titer generation of the innate immune response, we analyzed the adaptive immune response elicited by cBEV. Murine lymphocytes were isolated to assess DC maturation in response to our cBEV vaccine. The analysis of major antigen-presenting cell DC markers, CD80 and CD86, unveiled a significant augmentation in their expression upon treatment with cBEV (Figure 4e,f). In comparison, MnO_2 alone had a minimal effect on DCs, indicating that immune activation by cBEV was largely mediated by the immunogenicity of BEV, which contained immunostimulatory molecular patterns. Furthermore, the splenocytes isolated from the cBEV vaccines group showed the highest percentage of $CD8^+$ T cells (41.1%), which was 2.39-, 1.02- and 2.28-fold higher than that in the PBS (17.2%), BEV

(40.2%) and MnO_2 group (18.0%), respectively, suggesting an elevated degree of T activation (Figure S12). This sufficient T-cell activation would be beneficial for the tumor cell necrosis and inhibition.

Having confirmed that the cBEV enabled DCs and T cell activation for antibacterial in vivo, we further assessed the prophylactic ability of the cBEV vaccine in inhibiting tumor occurrence. To this end, mice were challenged with MCF-7 tumor cells and live *B. fragilis* after the cBEV treatment (Figure 4a). As shown in Figure 4g and 4h, the tumor volume grew rapidly in the non-treated groups. Whereas, cBEV vaccination before rechallenge effectively delayed the MCF-7 tumor growth. When compared with the PBS group, it was observed that MnO_2 alone resulted in only moderate tumor inhibition. Although native BEV also slowed down tumor growth, its efficacy was lower than that of cBEV. Consistently, quantitative data showed that cBEV-vaccinated mice tumor weight was significantly reduced compared to those in the BEV and MnO_2 groups (Figure S13a). The tumor growth inhibition (TGI) response of cBEV (76%) was outperformed by that of MnO_2 (29%) and BEV (55%) (Figure S13b). This enhanced effect could be attributed to the synergistic interplay between antigen-specific immunity and the activation of the STING pathway. In addition, the immunofluorescence images revealed that when BEV and MnO_2 were administrated individually, they produced only a modest increase in the population of intratumoral $CD8^+$ T cells (Figure 4i). In contrast, cBEV significantly promoted the infiltration of $CD8^+$ T within the tumor and exhibited the most potent tumor inhibition efficacy. The hematoxylin and eosin (H&E) staining images of the tumor revealed that cBEV treatment resulted in more extensive tumor necrosis with few nuclear staining (Figure 4i, inserted). We further enumerated the *B. fragilis* content in the tumors (Figure 4j). Consistently, mice immunized with cBEV exhibited a significantly lower bacterial count. This also coincided with

the significant inhibition of the tumor volume as compared to the cBEV group, which was remarkably higher than the MnO_2 and the control. Collectively, these results suggested that cBEV effectively enhanced the antitumor efficacy as a prophylactic bacterial vaccine.

cBEV improves the anticancer activity of anti-PD-L1 antibody

Increasing studies highlighted the favorable involvement of Mn^{2+} in amplifying STING activation, thus influencing the activation of DCs in the context of tumor immunotherapy.[33,36] Additionally, recent discoveries in tumor-associated bacteria suggest that commensal bacteria can stimulate antitumor immune responses through cross-reactivity.[37] In light of these, we next asked the ability of cBEV to enhance antitumor immunity for breast tumor and assess their effectiveness in synergizing with immune checkpoint blockade therapy, for example, anti-PD-L1 antibody. The mice were first subcutaneously injected with PBS or cBEVs three times, followed by intraperitoneal injection of anti-PD-L1 antibody twice (Figure 5a). Although anti-PD-L1 antibody failed to control the tumor growth, cBEV markedly inhibited the tumor progression, and a combination of cBEV and anti-PD-L1 (cBEV+anti-PD-L1) further suppressed the tumor growth, resulting in a more pronounced tumor retardance (Figure 5b,c). As revealed by tumor volumes (Figure 5d and Figure S14a), while the cBEV and anti-PD-L1 antibody-treated group only inhibited tumor growth at the early stage of treatment, the combination of cBEV and anti-PD-L1 antibody treatment effectively suppressed tumor growth tendency The insert immunofluorescence images suggested that cBEV and anti-PD-L1 antibody combination significantly enhanced the $CD8^+$ T-cell number in tumor tissues, consistent with the pronounced tumor inhibition performance. As shown, anti-PD-L1 alone resulted in poor tumor inhibition efficacy because of tumor immunosuppression. The tumor growth inhibition (TGI) response of

cBEV and anti-PD-L1 antibody combination was calculated to be 68%, outperforming that of anti-PD-L1 antibody (33%) and cBEV (49%), suggesting that combined treatment of cBEV and anti-PD-L1 antibody generated stronger synergistic tumor inhibition than either cBEV or anti-PD-L1 antibody (Figure S14b). Hematoxylin and eosin (H&E) staining further confirmed the effective inhibition of tumor cell proliferation in the combined cBEV and anti-PD-L1 antibody treatment group (Figure 5e). In addition, cBEV plus anti-PD-L1 antibody treatment showed improved expression levels of DC and T cell activation-related cytokines including TNF-α, IFN-γ, IFN-β, IgG and decreased levels of anti-inflammation cytokines such as IL-10 in serum (Figure 5f and Figure S15). The anti-metastatic effect of the combination treatment was further assessed. Consistent with tumor volume results, H&E-stained lung sections demonstrated that while cBEV elicited moderated metastatic tumor inhibition, the combination of cBEV and anti-PD-L1 antibody group showed fewer lung metastatic nodules, suggesting an enhanced suppression of cancer metastasis (Figure 5g, Figure S14c). As expected, the cBEV and anti-PD-L1 antibody combination markedly extended the survival time to 50 days without death of tumor-inoculated mice in comparison with mice treated by PBS (Figure S14d).

The content of *B. fragilis* in mice tumors after different treatments was evaluated by culturing the bacteria extracted from the tumor tissue. As compared to the PBS control, cBEV significantly decreased *B. fragilis* colony (Figure 6a,b and Figure S16). When further used in combination with anti-PD-L1 antibody, a high antibacterial efficacy of about 99% was achieved, with the colony numbers decreased to below 105 colony-forming units (CFU). To further evaluate the innate immune response of the treatments, the blood after treatments was collected for analysis. We found the combination of cBEV and anti-PD-L1 treatment generated higher IgG antibody titer and more $CD19^+$ B cells, suggesting effective humoral immunity (Figure 6c,d).

The subsequent DC activation in vivo was further investigated by collecting tumor-draining lymph nodes (TDLNs) for flow cytometry analysis. While cBEV and anti-PD-L1 antibody alone showed a moderate effect on DC maturation ($CD80^+CD86^+$), it was found that the combination of cBEV and anti-PD-L1 antibody treatment dramatically promoted DC activation from 19.9% to 42.2% (Figure 6e,f). Furthermore, although anti-PD-L1 treated alone resulted in a higher percentage of $CD8^+$ T cells from splenocytes compared with the control group, the adjunctive cBEV administration promoted this immune enhancement more significantly (Figure 6g,h). This increased T-cell activation allowed sufficient T-cell infiltrating into tumor tissue, significantly increasing the anticancer activity of anti-PD-L1 antibodies. Collectively, the reduction of *B. fragilis* colonization within the tumor and the activation of dendritic cells (DCs) mediated by Mn^{2+} both played pivotal roles in promoting T-cell infiltration. This, in turn, allowed anti-PD-L1 treatment to amplify T-cell immunity, thereby bolstering the efficacy of immunotherapy.

Conclusion

In this study, we developed an activatable nanointerface involving the encapsulation of commensal *B. fragilis*-derived BEVs within a responsive nanocloak. This approach aimed to enhance immunoreactivity with excellent biocompatibility in the context of breast cancer. Our findings revealed that the interfacial programming of BEVs effectively mitigates serious systemic side effects, establishing a crucial advancement in the quest for improved therapeutic strategies. Moreover, this approach facilitated the proficient delivery of antigens to the lymph nodes, enhancing the overall efficacy of the immunization process upon in vivo administration. Additionally, our study highlighted the remarkable immunogenicity exhibited by the interfacially cloaked vaccines. This heightened immunogenicity was attributed to the responsive

disintegration of the nanocloak. The intracellularly released Mn^{2+} advances DCs maturation through the activation of STING pathway. The successful circumvention of systemic side effects and the augmented immunogenicity underscore the potential of this responsive immunointerface in advancing breast cancer immunotherapy. Further exploration and validation through more breast cancer model and different subtypes will be needed to fully elucidate the translational and therapeutic implications of this commensal bacteria-targeted strategy in the realm of breast cancer treatment.

Experimental Section

Materials

K_2MnO_4 and polyvinyl pyrrolidone were purchased from Sigma-Aldrich (Saint Louis, USA). Phosphate buffered saline (PBS), Dulbecco's Modified Eagle Medium (DMEM), Roswell Park Memorial Institute 1640 (RPMI 1640) medium and fetal bovine serum (FBS) were purchased from Sigma-Aldrich (Saint Louis, USA). The BCA protein assay kit was purchased from Thermo Fisher Scientific (Waltham, USA). Murine IL-4 and GM-CSF were purchased from Abcam (Cambridge, England). ELISA kits for IFN-β and CXCL10 analysis were obtained from eBioscience (San Diego, USA). ELISA kits for IL-6, TNF-α, IL-1β, IL-10 and IFN-γ analysis were obtained from 4A Biotech Co. Ltd (Suzhou, China). ELISA kits for IgG were purchased from CAMILO Bioengineering Co. Ltd. (Nanjing China). Phospho-TMEM173/STING and phospho-IRF3 antibodies were purchased from Affinity Biosciences (USA). Mouse antibodies against APC/Cyanine7-CD3, Percp/Cyanine5.5-CD8a, APC-CD86, PE-CD80, PE/Cyanine7-CD11c and anti-mouse CD19-Percp/Cyanine5.5 were purchased from BioLegend (San Diego,

USA). D-Luciferin potassium was purchased from Beyotime (Shanghai, China). Other chemicals were purchased from Beyotime (Shanghai, China) unless otherwise noted.

Cell Lines and Bacterial Strains

Breast cancer cell lines MCF-7-luc cells were purchased from the ATCC and maintained at 37°C in 5% CO_2. Cells were used for experiments within 10 to 20 passages from thawing. *Bacteroides fragilis* (*B. fragilis*) strain 86-5443-2-2 was cultured anaerobically at 37°C. Bacterial culture substrates were discarded and resuspended in the PBS buffer (without calcium and magnesium) for mouse inoculation.

Design and synthesis of cBEV nanoarchitectures

Bacteroides fragilis-derived EVs (BEVs) were obtained by differential centrifugation. Bacterial culture supernatant was centrifuged at 500 g 10 min, 10, 000 g 90 min to remove the bacteria and bacterial debris. Then the supernatant was collected and centrifuged at 100, 000 g for 2 h to obtain the BEVs in the precipitation. We resuspended the BEVs in PBS and stored at -80 ℃ for further study. For microfluidic platform-based cBEV nanostructure synthesis, a classic spiral channel was designed and employed to synthesize BEV@MnO_2 (cBEV) nanoarchitectures. The chip was fabricated by 3D printing with the parameters of 35 mm long × 20 mm wide × 5 mm high. For the reaction in microfluidics, 10 μg of BEVs dispersed in polyvinyl pyrrolidone solution (1mM) and 0.1 mM $KMnO_4$ aqueous solution were introduced into the two inlets to the microfluidic chip separately to allow reaction. Full cBEV can be obtained by washing with dH_2O and centrifuging at 8000 g for 3 times.

Characterization of cBEV

To examine the morphology of BEVs, 10 μL of the BEV suspensions were placed on copper grids (Zhongjingkeyi Technology Co., Ltd, Beijing) and then negatively stained with 1% uranyl acetate three times. The morphologies of BEVs and cBEV were characterized by TEM (HITACHI, HT7700, Japan). Particle sizes were determined by nanoparticle tracking analysis (NTA, Particle Metrix Zetaview, Germany). Hydrodynamic sizes and zeta-potentials of all the nanoparticles were measured using a Malvern Zetasizer Nano ZS (Malvern Instruments). All the samples are 1,000 times diluted before measurement. Cell viability was measured by CCK-8 dye reduction assay. The percentages of live cells were calculated and plotted using Prism software (GraphPad Prism).

Cellular uptake of BMDCs

Bone marrow-derived dendritic cells (BMDCs) were harvested from bone marrow cells flushed from the C57BL/6 mice and dispersed in BMDCs medium: RPMI 1640 medium containing 10% FBS, GM-CSF (20 ng mL^{-1}) and IL-4 (10 ng mL^{-1}). The internalization of cBEVs by BMDCs was monitored by CLSM (confocal laser scanning microscope) and flow cytometry, and the quantification analysis used image J and ICP-OES. Cells were seeded in 6-well plates (2.5×10^6 cells per well) and confocal dishes were cultured for overnight. 8.5 μg mL^{-1} of BEV, 41.5 μg mL^{-1} of MnO_2 and 50 μg mL^{-1} cBEV with fresh medium were added and further incubated for 4h at 37°C. The fluorescence intensities of DiD fluorescent probe were measured by CLSM. Nontreated cells were set as the control group. A NovoCyte FACS flow cytometer (ACEA Biosciences, Inc.) was used to measure the fluorescence intensity with excitation and emission wavelengths at 635 nm, respectively. Then, cells were further collected and digested to detect the concentrations of Mn^{2+} in BMDCs by ICP-MS.

In vivo prophylactic efficiency of the cBEV vaccines.

We first tested the prophylactic efficiency of the cBEV vaccines against MCF-7 tumor. On day 21, 2×10^6 of MCF-7 cells were subcutaneously injected into the mice and 10^7 of colony-forming units (CFU) *B. fragilis* were intratumally injected 7 days later. The tumor growth was monitored regularly by measuring the tumor length and width. Tumor volume was calculated according to the formula: $V = (L \times W \times W)/2$ (L, the longest dimension; W, the shortest dimension). TGI was calculated by the formula: $TGI = (1- T_t/C_t)*100\%$, where T_t = tumor weight of treated group at time t, C_t = tumor weight of PBS group at time t. The tumors were collected and embedded for hematoxylin and eosin (H&E) staining and immunofluorescence analysis.

We evaluated the innate immune response induced by cBEV vaccines. Different groups of PBS, BEV, MnO_2 and cBEV were subcutaneously injected at day 0, day 7 and day 14. At day 15, lymph nodes and spleens were collected and digested to obtain a single-cell suspension and the cells were stained with anti-mouse CD19-Percp/Cyanine5.5 (Biolegend, cat. no 115533, clone 6D5) and then subjected to flow cytometry. Meanwhile, the serum was detected with the following ELISA kits (CAMILO Bioengineering Co. Ltd., Nanjing): IgG. Furthermore, the splenocytoes were stained with mouse antibodies against APC/Cyanine7-CD3, Percp/Cyanine5.5-CD8a (BioLegend; San Diego, USA) for flow cytometry analysis.

Antitumor activity of the combination of cBEV vaccines and anti-PD-L1 antibody

2×10^6 of MCF-7-luc cells were subcutaneously injected into the balb/c mice at day 0. When the tumor volume of MCF-7-luc tumor-bearing mice reached 80-100 mm^3, the mice were injected subcutaneously with cBEV at the dosage of 6.5 mg kg^{-1} at day 8, 10 and 12 in the presence or absence of intraperitoneal injection of anti-PD-L1 antibody at the dosage of 100 μg per mouse at

day 9 and 11. Tumor growth was regularly monitored by bioluminescence imaging using in vivo bioluminescence IVIS Spectrum system and Living Image software (IVIS Lumina K Series) after 10 min of the injection of D-Luciferin (150 mg/kg). The exposure time was 2 min. In all experiments, animals were considered as sacrificed when their tumor volumes exceeded 1,000 mm3. After treatment, the mice were sacrificed and the spleen, lymph nodes and tumors were collected. For DCs expression, lymph nodes were digested to obtain a single-cell suspension. The cells were stained with CD11c-PE/Cyanine7 (Biolegend, cat. no 117318, clone N418), anti-mouse CD80-PE (Biolegend, cat. no 104708, clone 16-10A1), anti-mouse CD86-APC (Biolegend, cat. no 105012, clone GL-1) and anti-mouse CD19-Percp/Cyanine5.5 (Biolegend, cat. no 115533, clone 6D5) and then subjected to flow cytometry. For T-cell expression, spleens were ground to get the single-cell suspension, the ACK lysing buffer was used to remove red blood cells. Then the cells were stained with anti-mouse CD3-APC/Cyanine7, anti-mouse CD8a-Percp/Cyanine5.5, anti-mouse CD4-PE (Biolegend) and then subjected to flow cytometry. Fluorescent signals were assessed using a NovoCyte FACS flow cytometer (ACEA Biosciences, Inc.) and analyzed with Flowjo software. The tumors were collected, weighed and then digested for 1 hour at 37 ℃ in RPMI containing collagenase (0.5 mg mL^{-1}), 2.5 mg mL^{-1} Liberase TL and DNA enzyme (Miltenyi Biotec, 0.1 mg mL^{-1}) and then filtered through 40-μm cell strainers to get the single-cell suspensions. The bacterial content of the tumor site was evaluated at by the agar plate dilution method. Colonies were harvested by scraping, with 0.9% NaCl as vehicle, and Mycobacterium concentrations were calculated according to the McFarland Standards method. Colony-forming unit (CFU) values were calculated from the optical absorbance of bacterial suspensions at 600 nm. To quantify bacterial load, the homogenates were serially diluted in PBS, and 50 μL of each dilution was plated onto TSB agar plates. The number of colonies was

counted after incubation overnight at 37 ℃. The lungs were washed and fixed with 4% PFA for 48 h. Besides, the number of lung tumor metastases was calculated and prepared for hematoxylin and eosin (H&E) staining. The serums were harvested for ELISA analyses to measure the concentration of IFN-β, TNF-α, IFN-γ, IL-1β, IgG and IL-10.

Statistical Analysis

Measurements of micrographs and IHC quantitation were done using Leica Aperio ImageScope, Leica Biosystems. Statistical analyses were done using GraphPad Prism 5. Results were considered to be statistically significant if $P < 0.05$. The error bar around each data point is the SD. Tukey's multiple comparisons test was used to calculate the statistical significance. *$P < 0.05$, **$P < 0.01$, ***$P < 0.001$, ****$P < 0.0001$. Results were expressed as mean ± SE between triplicate experiments performed thrice. For comparison between multiple groups, statistical significance was determined by one-way ANOVA and Bonferroni analysis. Comparison between the two groups was done using the Student t-test.

FIGURES

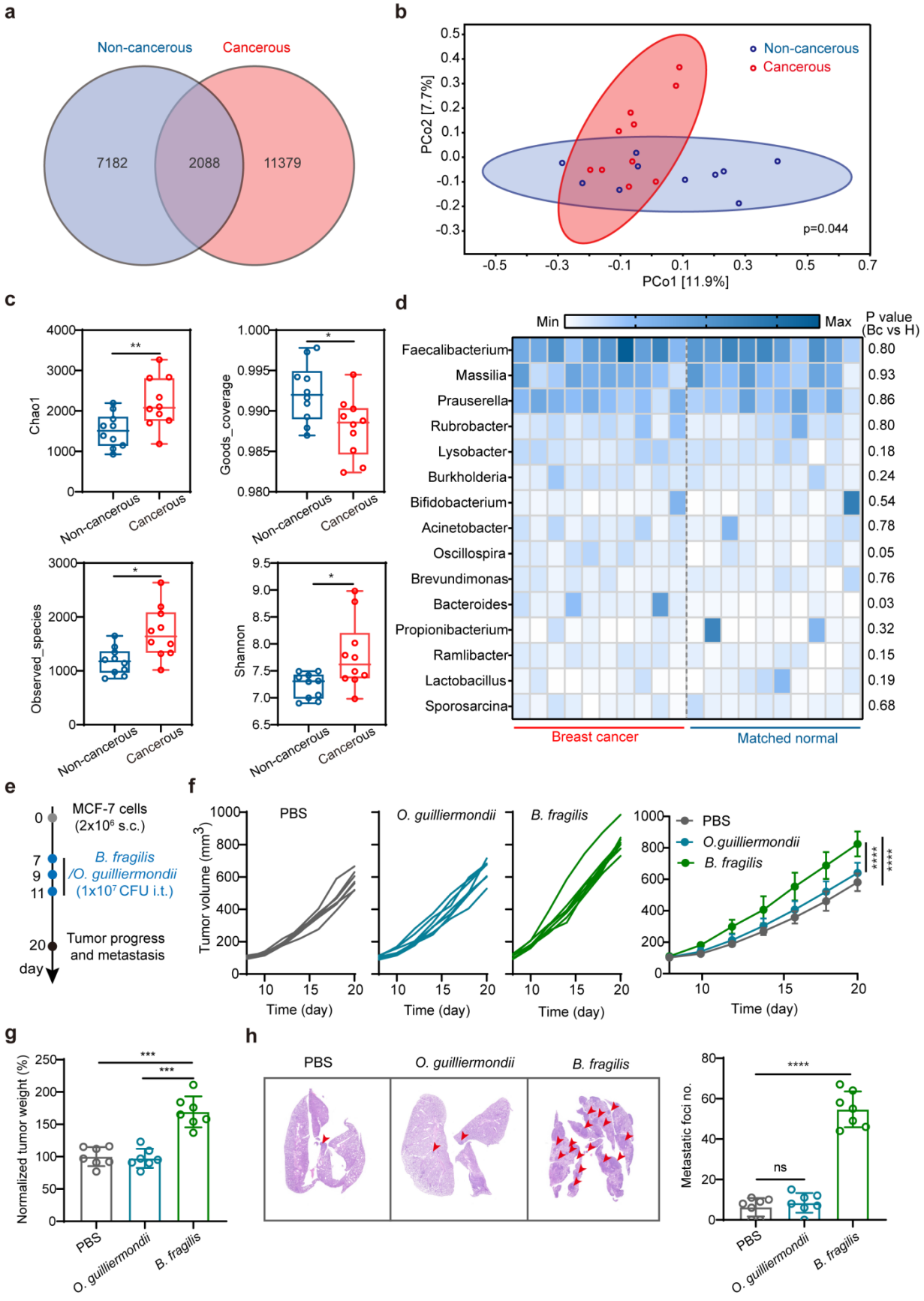
a
Non-cancerous
Cancerous
7182
2088
11379
b
Non-cancerous
Cancerous
PCo2 [7.7%]
PCo1 [11.9%]
p=0.044
c
Chao1
Goods_coverage
Observed_species
Shannon
Non-cancerous
Cancerous
d
Min
Max
P value (Bc vs H)
Faecalibacterium 0.80
Massilia 0.93
Prauserella 0.86
Rubrobacter 0.80
Lysobacter 0.18
Burkholderia 0.24
Bifidobacterium 0.54
Acinetobacter 0.78
Oscillospira 0.05
Brevundimonas 0.76
Bacteroides 0.03
Propionibacterium 0.32
Ramlibacter 0.15
Lactobacillus 0.19
Sporosarcina 0.68
Breast cancer
Matched normal
e
MCF-7 cells (2x10⁶ s.c.)
B. fragilis /O. guilliermondii (1x10⁷ CFU i.t.)
Tumor progress and metastasis
day
f
PBS
O. guilliermondii
B. fragilis
Tumor volume (mm³)
Time (day)
g
Normalized tumor weight (%)
h
Metastatic foci no.
ns

Figure 1. Commensal *Bacteroides fragilis* promotes the progression of human breast tumor. (a) Venn diagram of detected microbial bacterial abundance in benign tissues and cancerous tissues from patients with breast cancer. (b) Principal component analysis (PcoA) (P= 0.044) of detected bacterial operational taxonomic units (OTUs) in non-cancerous tissues and cancerous tissues from patients with breast cancer. Each point represents each people (n = 10). (c) The estimation of human breast microbial community base on Chao1 diversity index, Goods coverage index, observed species and Shannon diversity index in non-cancerous and cancerous tissues. Data are presented as means ± SEM (n =10). (d) Genus-level relative microbial abundance of breast cancer and matched normal tissues. (e) Schemes of the experiment design. The BALB/c mice were injected with MCF-7 breast tumor cells (2×10^6 per mouse). At days 7, 9, 11, the MCF-7 tumor-bearing mice were injected with *B. fragilis* or *O.guilliermondii* (10^7 CFU per mouse). (f) Individual and average tumor growth curves for MCF-7 tumors on mice after the various treatments indicated. (g) Quantitative analysis of nomoralized tumor weight of mice with different treatments. All of the other groups were normalized to the PBS group. (h) Representative H&E images of lungs in each group and the corresponding quantification of nomoralized lung metastatic nodules in each group. The arrows indicated metastatic tumors (n=7). Representative images per treatment group are shown. Data are means ± SEM. Statistical significance was calculated by one-way ANOVA test. *P < 0.05, **P < 0.01, ***P < 0.001, ****P< 0.0001, ns denotes no significant difference.

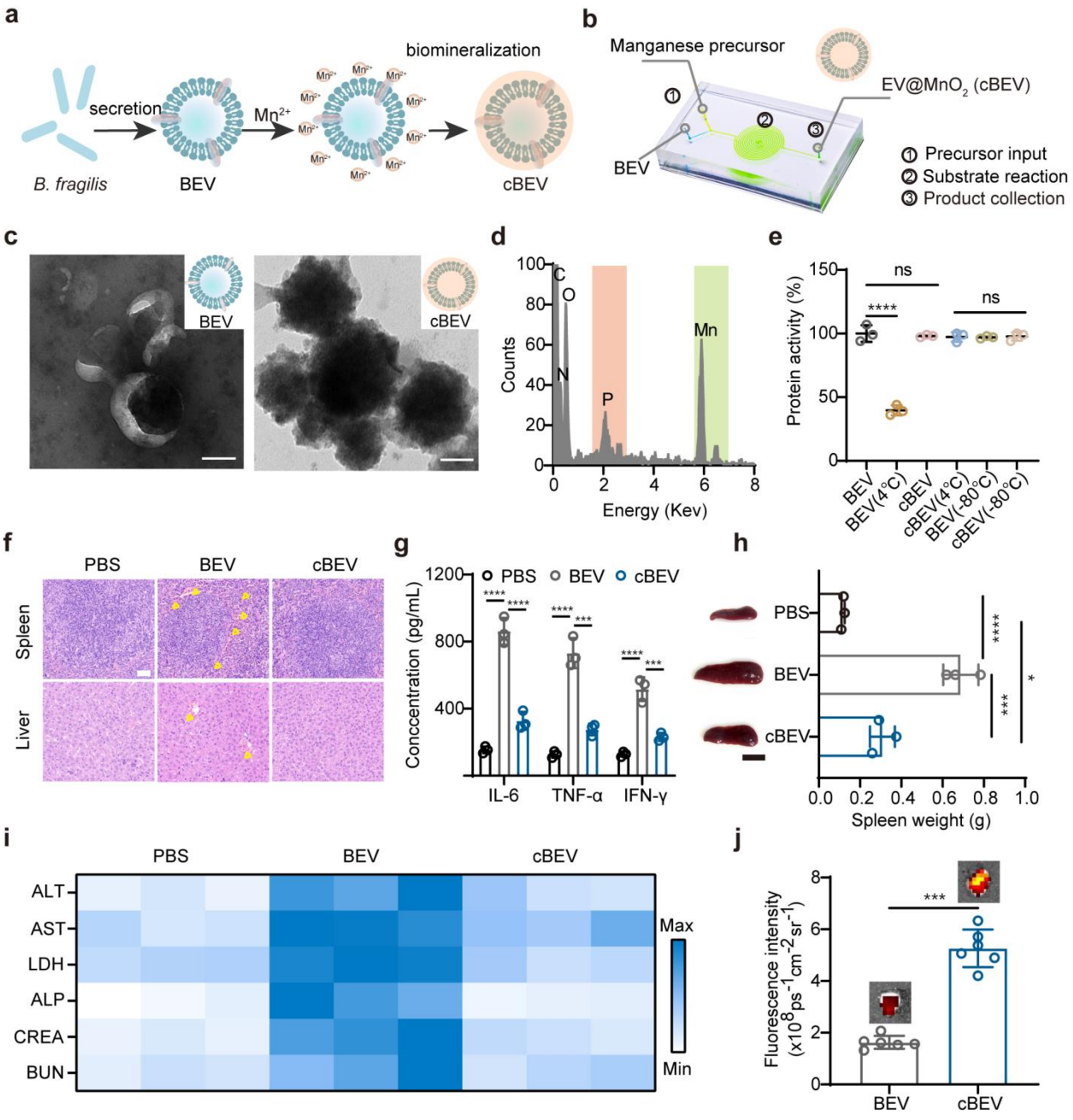

Figure 2. Design and biosafety assessments of nanocloaked cBEV.(a,b) Schematic illustration of steps for cBEV synthesis. All the preparation was carried out on-chip under easy and mild aqueous conditions, allowable for scalable synthesis. (c) TEM images of BEVs and the prepared nanocloaked cBEV (scale bar: 50 nm). (d) Analyses of elemental distribution by EDX spectrum of the obtained cBEV nanoparticles. (e) Stability investigation based on the size of BEVs and

cBEVs at different temperatures. All of the other groups were normalized to the naive BEV group. (f) H&E staining of spleen and liver after cBEV treatments. Scale bar: 200 μm. The yellow arrows indicated the potential inflammatory infiltration. (g) Systemic cytokines release (IL-6, TNF-α and IFN-γ) after BEVs and cBEV injection. (h) Representative images of spleens in each group after receiving different treatments and corresponding mass weight. (i) The serum biochemical indexes of ALT, AST, LDH, ALP, CREA and BUN concentration in the vaccinated mice at different time points determined by ELISA. The means the actual number of Min and Max signs was 0.1 and 1.0, respectively. The mice treated with PBS were set as the control group. All of the treated groups were normalized to the control group. (j) Representative fluorescence images of the lymph nodes in the MCF-7-tumor-bearing mice 24 h after s.c. injection with DiR-labeled BEVs and cBEV and the corresponding fluorescence intensity accumulated at lymph node. The meaning the actual number of Min and Max signs was 4.59e7 and 1.04e8, respectively. Representative images per treatment group are shown. Data are representative of at least three independent experiments. Data are means ± SEM. Statistical significance was calculated by one-way ANOVA test. *P < 0.05, **P < 0.01, ***P < 0.001, ****P< 0.0001, ns denotes no significant difference.

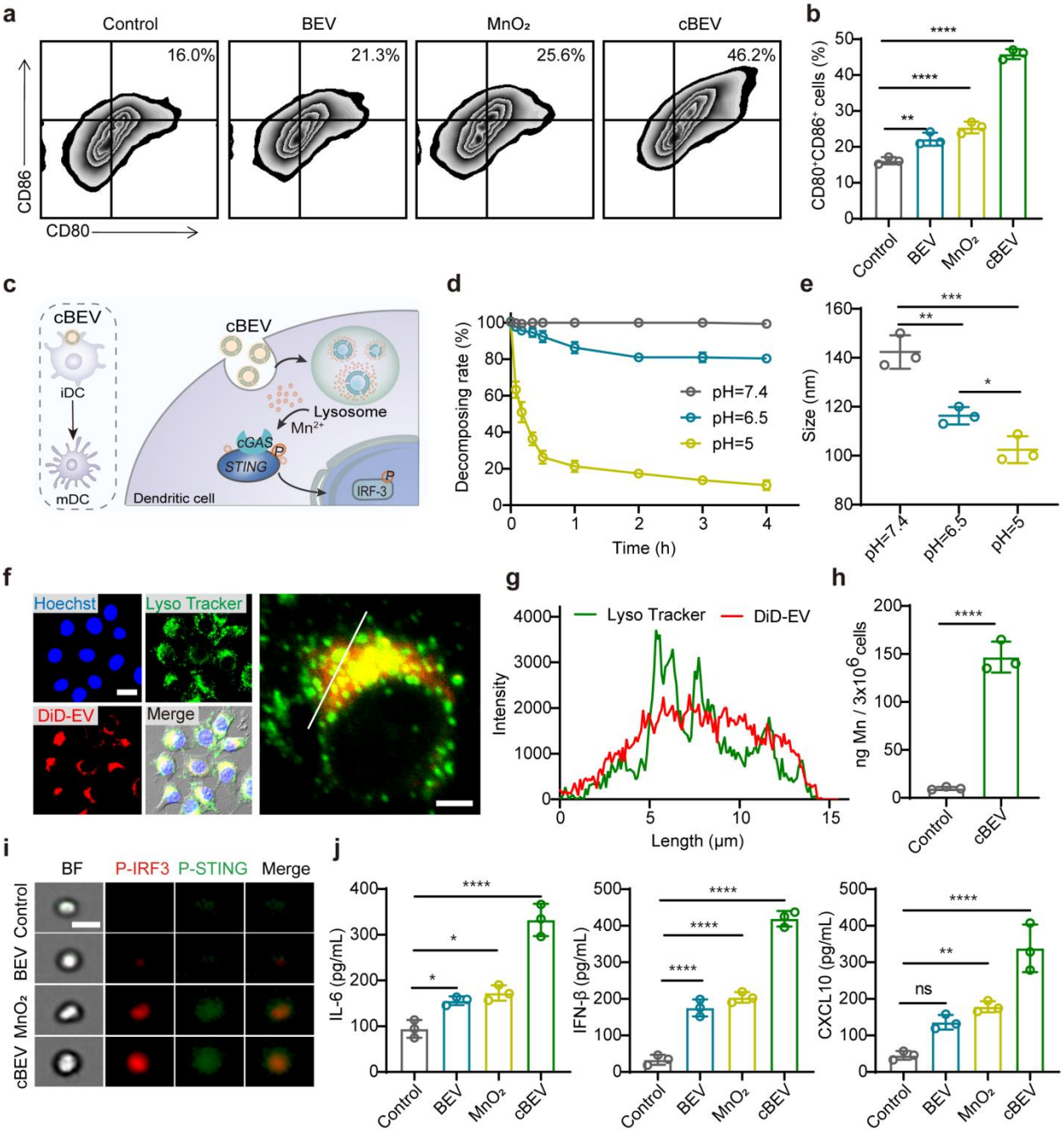

Figure 3. Cloaked BEV improves DC maturation via activating STING pathway.(a,b) Representative flow cytometry plots (a) and quantification (b) of matured DCs ($CD80^+CD86^+$) after treatments. (c) Schematic illustration of the DC activation mediated by cBEV. cBEV was internalized into BMDCs and then following intracellular exposure of manganese ion (Mn^{2+}), the

free Mn^{2+} released in the cytosol could sensitize cGAS to bacterial-derived cytosolic dsDNA, facilitating the STING pathway activation and DC maturation. (d) The degradation level was determined by quantifying free Mn^{2+} via ICP-OES. cBEV was incubated with different acidic aqueous conditions, it was relatively stable under pH condition of 6.5 (mimicking the pH value of tumor microenvironment), while it was quickly degraded under lysosomal conditions (pH=5). (e) Hydrodynamic size changes of cBEV under the mocked lysosomal conditions (n = 3) measured by dynamic light scattering (DLS). (f) Internalization analysis of cBEV (DiD-labeled BEV; red) in BMDCs (lysosome; green) by confocal microscopy (4-hour incubation), Scale bars, 20 μm. (g) Colocalized images of BEV with the lysosomal compartments and the quantitative analysis of the colocalization coefficient of BEV and lysosomes. Scale bars, 5 μm. (h) Cellular uptake of cBEV in BMDCs determined by measuring the Mn^{2+} concentrations through ICP-MS. (i) Amnis Imagestream imaging cytometry analysis of cBEV-mediated STING pathway activation in BMDCs. Scale bar, 20 μm. (j) Chemokines concentrations of IL-6, IFN-β and CXCL10 secreted in BMDC supernatants after incubation with cBEV overnight. Representative images per treatment group are shown. Data are representative of at least three independent experiments. Data are means ± SEM. Statistical significance was calculated by one-way ANOVA test. *P < 0.05, **P < 0.01, ***P < 0.001, ****P< 0.0001, ns denotes no significant difference.

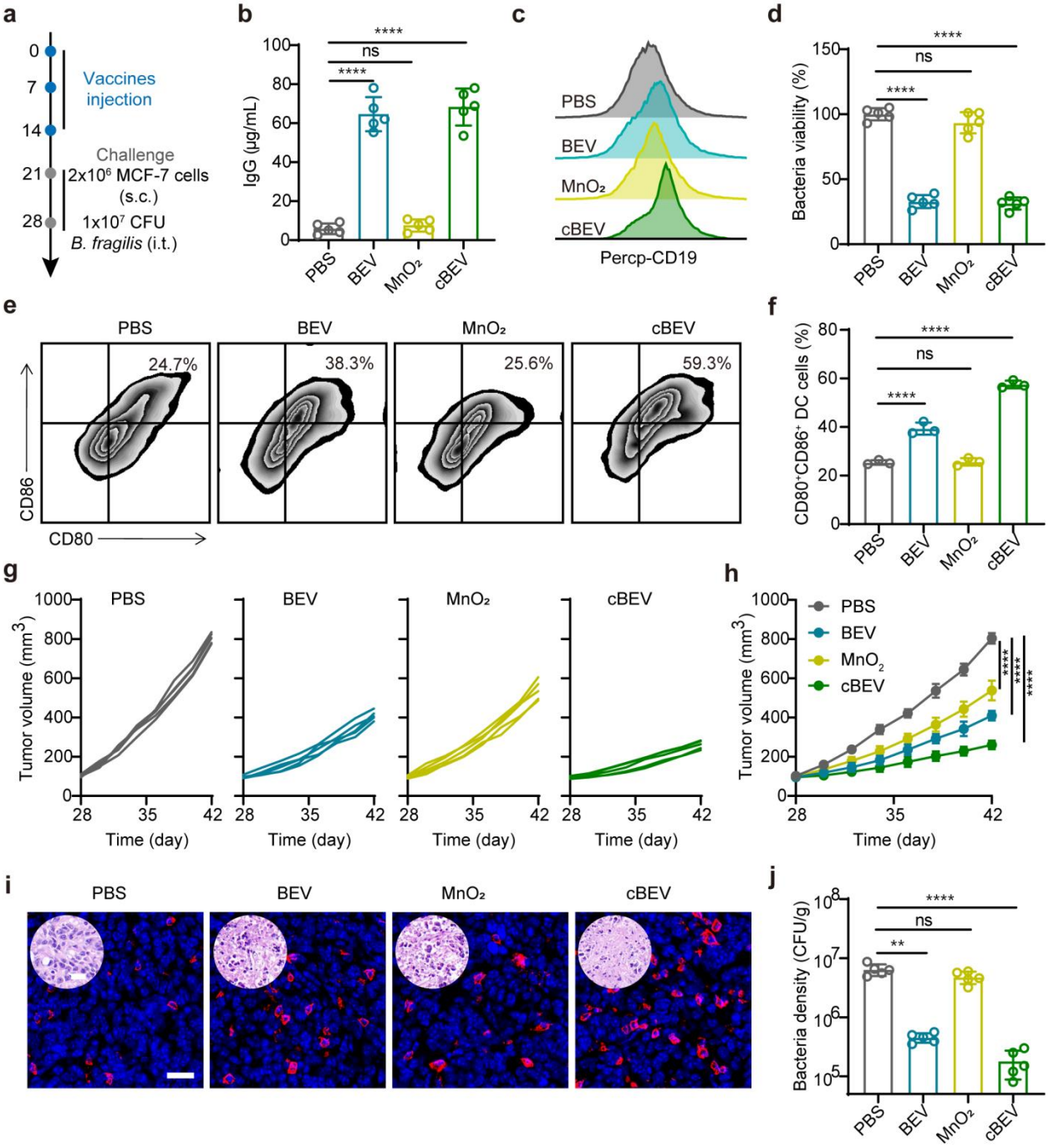

Figure 4. Prophylactic efficacy of subcutaneous injected cBEV against MCF-7 breast tumor challenge. (a) Schemes of the tumor challenge experiment design. Mice were subcutaneously immunized with various vaccine formulations (PBS, BEV, MnO_2 or cBEV), and then challenged with MCF-7 breast tumor cells (2×10^6 per mouse) at day 21.7 days later, the MCF-7 breast

tumor-bearing mice were intratumorally injected with *B. fragilis* (10^7 CFU per mouse). (b) Serum IgG levels of mice 7 days after vaccinating with cBEV determined by ELISA. (c) Representative flow cytometry plots of $CD19^+$ B cells in the lymph nodes after vaccination. (d) Viability of *B. fragilis* after incubation for 1 h with the sera collected from naive or cBEV vaccinated mice. All of the treated groups were normalized to the PBS group. (E,F) Representative flow cytometry plots (e) and quantification (f) of $CD80^+CD86^+$ DC cells in the lymph nodes after previously vaccinated. (g,h) Individual (g) and average (h) tumor growth curves for MCF-7 tumors on mice after the various treatments indicated. Growth curves represent means ± SEM. (i) Representative fluorescence images of the tumor-infiltrating $CD8^+$ T cells in each group of tumors collected from MCF-7 tumor-bearing mice after treatments. Scale bar: 50 μm. The insert graph shows the representative H&E images. Scale bar: 20 μm. (j) Quantitative analysis of *B. fragilis* bacterial colonies in MCF-7 tumor-bearing mice vaccinated with cBEVs. Representative images per treatment group are shown, n= 5 biologically independent mice for each group. Data are means ± SEM. Statistical significance was calculated by one-way ANOVA test. *P < 0.05, **P < 0.01, ***P < 0.001, ****P< 0.0001, ns denotes no significant difference.

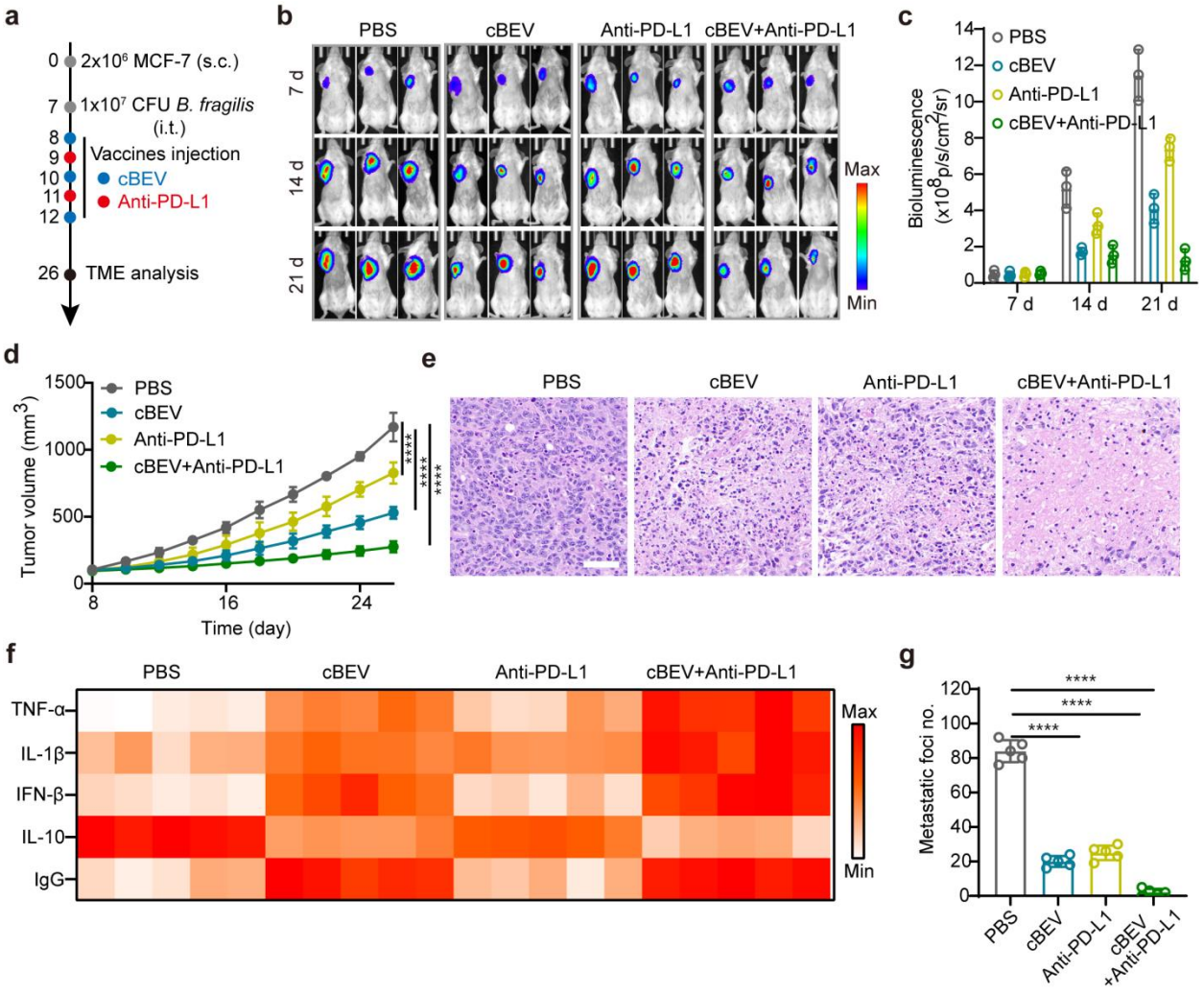

Figure 5. cBEV nanovaccine synergized with anti-PD-L1 therapies inhibit tumor progression in MCF-7 tumor model. (a) Schematic timeline of the animal experiment. Female BALB/c mice (n = 5 mice per group) were subcutaneously (s.c.) inoculated with MCF-7-Luc breast tumor cells (2×10^6 per mouse). At day 7, the MCF-7-Luc breast tumor-bearing mice were intratumorally injected with *B. fragilis* (10^7 CFU per mouse). Subsequently, the mice were subcutaneously immunized with the indicated vaccine formulations (cBEV, 6.5 mg/kg) at days 8, 10, 12 and intraperitoneally injected with anti-PD-L1 antibody (5 mg/kg) at days 9, 11 when the tumors reached a volume of 80~100 mm^3. (b) In vivo bioluminescence images of mice bearing MCF-7-Luc tumors at different days. The actual mean of Min and Max signs was 1.95e6 and 4.37e7,

respectively. (c) Quantification of the bioluminescence intensity (n= 3). (d) Average tumor growth curves for MCF-7 tumors on mice after the various treatments indicated (n= 5 biologically independent mice for each group). Growth curves represent means ± S.E.M. (e) H&E-stained tumor lesions collected from MCF-7 tumor-bearing mice after treatments. Scale bar: 50 μm. (f) Heatmap of the level of TNF-α, IL-1β, IFN-β, IL-10 and IgG in the serum after different treatments determined by ELISA (n= 5). The actual mean of Min and Max signs was 0.1 and 1.0, respectively. The mice treated with PBS were set as the control group. All of the treated groups were normalized to the control group. (g) Quantification of lung metastatic nodules in each group (n= 5). Representative images per treatment group are shown. Data are means ± SEM. Statistical significance was calculated by one-way ANOVA with Bonferroni's multiple comparisons test for growth curves. *P < 0.05, **P < 0.01, ***P < 0.001, ****P< 0.0001, ns denotes no significant difference.

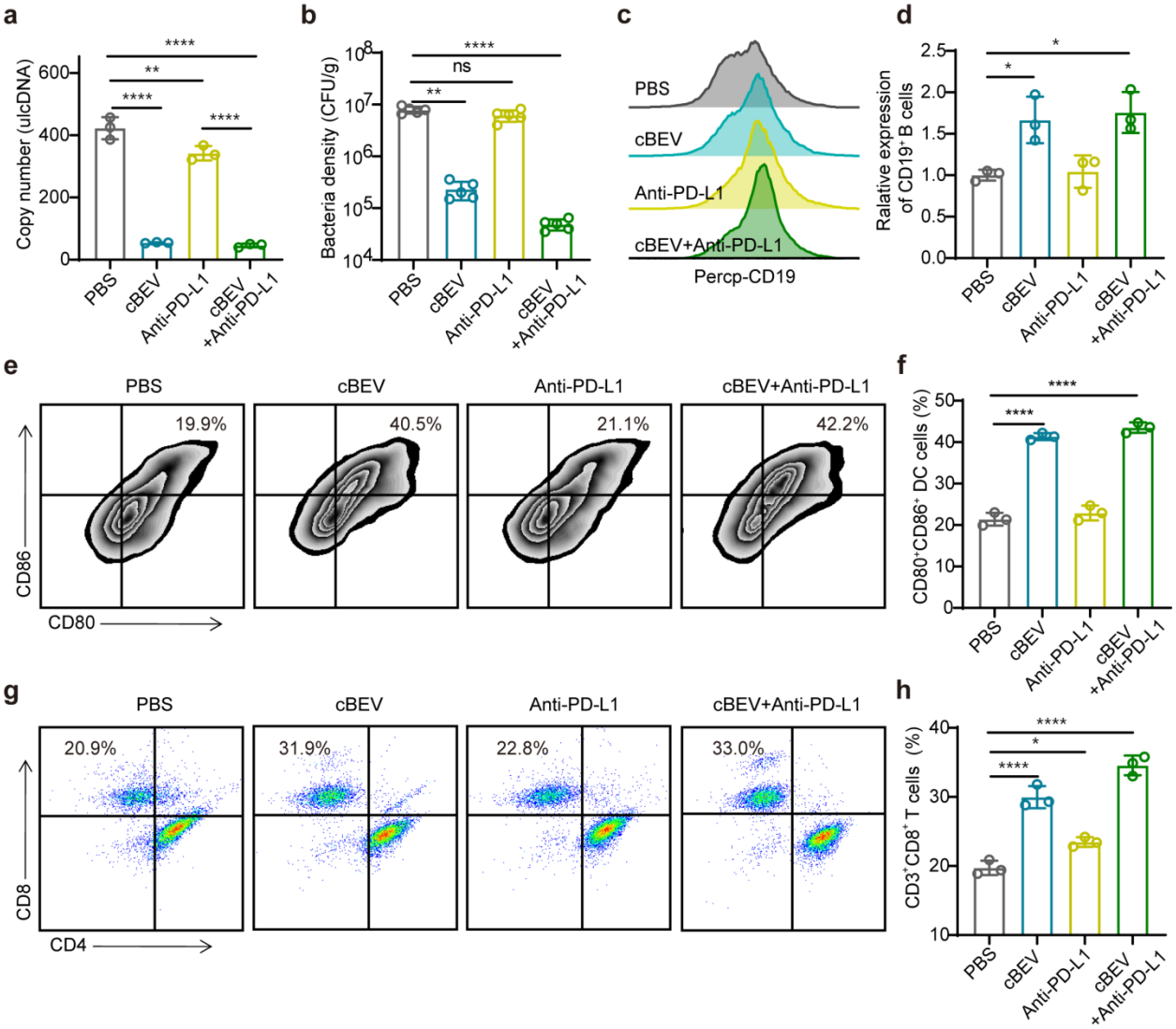

Figure 6. cBEV combined with anti-PD-L1 antibody for potent immune modulation. (a) Relative abundance of *B. fragilis* in MCF-7 breast tumor after treatments. (b) Quantitative analysis of *B. fragilis* bacterial colonies in tumor tissues of mice with different treatments. (c,d) Representative flow cytometry plots (c) and quantitative analysis (d) of $CD19^+$ B cells in the peripheral blood. All of the other groups were normalized to the control group. (e,f) Representative flow cytometry plots (e) and the corresponding quantification (f) of matured DCs ($CD80^+CD86^+$) in the lymph nodes. (g,h) Representative flow cytometry plots (g) and the corresponding quantitative analysis (h) of $CD3^+CD8^+$ T cells in the spleen. The experiment was performed at least three times. The

data are presented as the means ± SD. Statistical significance was calculated by one-way ANOVA test. *P < 0.05, **P < 0.01, ***P < 0.001, ****P< 0.0001, ns denotes no significant difference.

SCHEMES

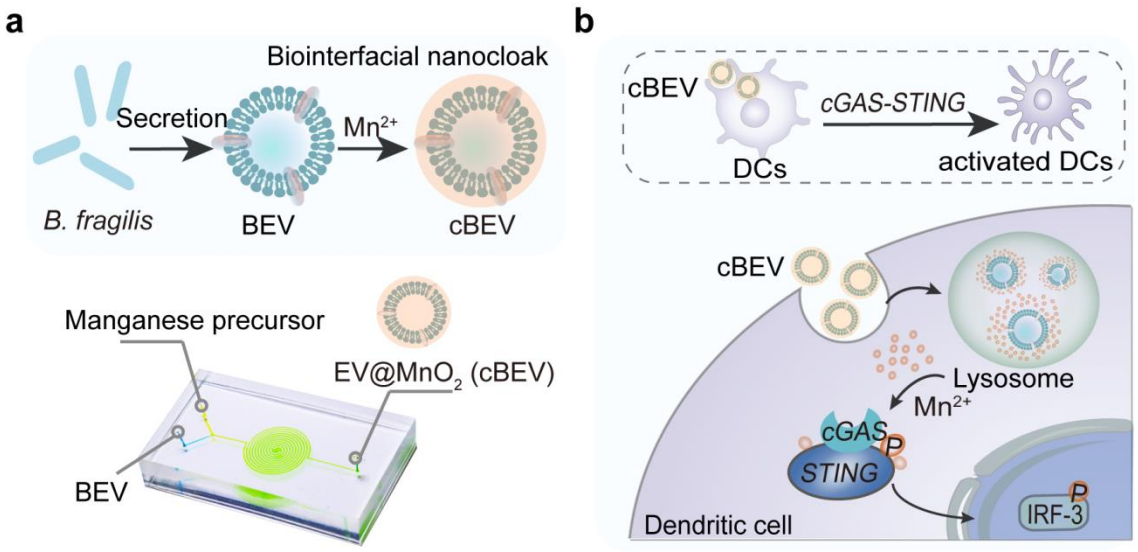

ASSOCIATED CONTENT

Data Availability Statement

All data are available in the main text or the supplementary materials.

Supporting Information

Figures S1-S16, including differential expression of *Bacteroides* and *Oscillospira* abundance (Figure S1), tumors images (Figure S2), the potential prevention ability of the BEV vaccines (Figure S3), side effects of BEV vaccines (Figure S4), characterizations of cBEV (Figure S5), biosafety test of cBEV in vitro (Figure S6), H&E staining images (Figure S7), toxicity assay in vivo (Figure S8), colocalization analysis (Figure S9), STING pathway activation (Figure S10), $CD19^+$ B cells expressed in lymph nodes (Figure S11), $CD3^+CD8^+$ T cells expression in the tumor (Figure S12), tumor weight and tumor inhibition efficiency (TGI) (Figure S13), anti-tumour effects of cBEV vaccines combined with anti-PD-L1 antibody in MCF-7 tumors-bearing mice (Figure S14), cytokines levels in the serum (Figure S15), plate photos of *B. fragilis* bacterial colonies (Figure S16).

AUTHOR INFORMATION

Corresponding Author

Xianguang Ding - State Key Laboratory of Organic Electronics and Information Displays & Jiangsu Key Laboratory for Biosensors, Institute of Advanced Materials (IAM), Nanjing University of Posts and Telecommunications, Nanjing 210023, China; Email: iamxgding@njupt.edu.cn

Lianhui Wang - State Key Laboratory of Organic Electronics and Information Displays & Jiangsu Key Laboratory for Biosensors, Institute of Advanced Materials (IAM), Nanjing University of Posts and Telecommunications, Nanjing 210023, China; Email:iamlhwang@njupt.edu.cn

Present Addresses

Jingjing Zhang - State Key Laboratory of Organic Electronics and Information Displays & Jiangsu Key Laboratory for Biosensors, Institute of Advanced Materials (IAM), Nanjing University of Posts and Telecommunications, Nanjing 210023, China

Shuangshuang Wan - State Key Laboratory of Organic Electronics and Information Displays & Jiangsu Key Laboratory for Biosensors, Institute of Advanced Materials (IAM), Nanjing University of Posts and Telecommunications, Nanjing 210023, China

Hao Zhou - Department of General Surgery, The First Affiliated Hospital of Soochow University, Suzhou, Jiangsu Province, China

Jiaxin Du - State Key Laboratory of Organic Electronics and Information Displays & Jiangsu Key Laboratory for Biosensors, Institute of Advanced Materials (IAM), Nanjing University of Posts and Telecommunications, Nanjing 210023, China

Yaocheng Li - State Key Laboratory of Organic Electronics and Information Displays & Jiangsu Key Laboratory for Biosensors, Institute of Advanced Materials (IAM), Nanjing University of Posts and Telecommunications, Nanjing 210023, China

Houjuan Zhu - A*STAR (Agency for Science, Technology and Research), Singapore 138634, Singapore

Lixing Weng - State Key Laboratory of Organic Electronics and Information Displays & Jiangsu Key Laboratory for Biosensors, Institute of Advanced Materials (IAM), Nanjing University of Posts and Telecommunications, Nanjing 210023, China

Author Contributions

JJZ, SSW and XGD designed the study. JJZ, JXD, YCL, HZ performed the research. HZ provided the clinical samples and health informations. JJZ, SSW, HJZ, LXW and LHW analysed the data. JJZ and XGD wrote the manuscript.

All the authors contribute to the manuscript.

Notes

The authors declare no competing financial interest.

ACKNOWLEDGMENT

This work was supported by the Leading-edge Technology Programme of Jiangsu Natural Science Foundation (BK20212012), Natural Science Foundation (22207056, 62288102) and the Natural Science Foundation of Jiangsu Province (BK20210580, BK20220384).

REFERENCES

(1) Garrett, W. S. Cancer and the Microbiota. *Science* **2015**, *348* (6230), 80-86.

(2) Lax, A. J. Bacterial Toxins and Cancer — a Case to Answer? *Nat. Rev. Microbiol.* **2005**, *3* (4), 343-349.

(3) Nejman, D.; Livyatan, I.; Fuks, G.; Gavert, N.; Zwang, Y.; Geller, L. T.; Rotter-Maskowitz, A.; Weiser, R.; Mallel, G.; Gigi, E.; Meltser, A.; Douglas, G. M.; Kamer, I.; Gopalakrishnan, V.; Dadosh, T.; Levin-Zaidman, S.; Avnet, S.; Atlan, T.; Cooper, Z. A.; Arora, R.; Cogdill, A. P.; Khan, M. A. W.; Ologun, G.; Bussi, Y.; Weinberger, A.; Lotan-Pompan, M.; Golani, O.; Perry, G.; Rokah, M.; Bahar-Shany, K.; Rozeman, E. A.; Blank, C. U.; Ronai, A.; Shaoul, R.; Amit, A.; Dorfman, T.; Kremer, R.; Cohen, Z. R.; Harnof, S.; Siegal, T.; Yehuda-Shnaidman, E.; Gal-Yam, E. N.; Shapira, H.; Baldini, N.; Langille, M. G. I.; Ben-Nun, A.; Kaufman, B.; Nissan, A.; Golan, T.; Dadiani, M.; Levanon, K.; Bar, J.; Yust-Katz, S.; Barshack, I.; Peeper, D. S.; Raz, D. J.;

Segal, E.; Wargo, J. A.; Sandbank, J.; Shental, N.; Straussman, R. The Human Tumor Microbiome Is Composed of Tumor Type–Specific Intracellular Bacteria. *Science* **2020**, *368* (6494), 973-980.

(4) Gopalakrishnan, V.; Helmink, B. A.; Spencer, C. N.; Reuben, A.; Wargo, J. A. The Influence of the Gut Microbiome on Cancer, Immunity, and Cancer Immunotherapy. *Cancer Cell* **2018**, *33* (4), 570-580.

(5) Liu, N. N.; Yi, C. X.; Wei, L. Q.; Zhou, J. A.; Jiang, T.; Hu, C. C.; Wang, L.; Wang, Y. Y.; Zou, Y.; Zhao, Y. K.; Zhang, L. L.; Nie, Y. T.; Zhu, Y. J.; Yi, X. Y.; Zeng, L. B.; Li, J. Q.; Huang, X. T.; Ji, H. B.; Kozlakidis, Z.; Zhong, L.; Heeschen, C.; Zheng, X. Q.; Chen, C.; Zhang, P.; Wang, H. The Intratumor Mycobiome Promotes Lung Cancer Progression Via Myeloid-Derived Suppressor Cells. *Cancer Cell* **2023**, *41* (11), 1927-1944.e1929.

(6) Parhi, L.; Alon-Maimon, T.; Sol, A.; Nejman, D.; Shhadeh, A.; Fainsod-Levi, T.; Yajuk, O.; Isaacson, B.; Abed, J.; Maalouf, N.; Nissan, A.; Sandbank, J.; Yehuda-Shnaidman, E.; Ponath, F.; Vogel, J.; Mandelboim, O.; Granot, Z.; Straussman, R.; Bachrach, G. Breast Cancer Colonization by Fusobacterium Nucleatum Accelerates Tumor Growth and Metastatic Progression. *Nat. Commun.* **2020**, *11* (1), 3259.

(7) Riquelme, E.; Zhang, Y.; Zhang, L.; Montiel, M.; Zoltan, M.; Dong, W.; Quesada, P.; Sahin, I.; Chandra, V.; San Lucas, A.; Scheet, P.; Xu, H.; Hanash, S. M.; Feng, L.; Burks, J. K.; Do, K.-A.; Peterson, C. B.; Nejman, D.; Tzeng, C.-W. D.; Kim, M. P.; Sears, C. L.; Ajami, N.; Petrosino, J.; Wood, L. D.; Maitra, A.; Straussman, R.; Katz, M.; White, J. R.; Jenq, R.; Wargo, J.; McAllister, F. Tumor Microbiome Diversity and Composition Influence Pancreatic Cancer Outcomes. *Cell* **2019**, *178* (4), 795-806.e712.

(8) Geller, L. T.; Barzily-Rokni, M.; Danino, T.; Jonas, O. H.; Shental, N.; Nejman, D.; Gavert, N.; Zwang, Y.; Cooper, Z. A.; Shee, K.; Thaiss, C. A.; Reuben, A.; Livny, J.; Avraham, R.; Frederick, D. T.; Ligorio, M.; Chatman, K.; Johnston, S. E.; Mosher, C. M.; Brandis, A.; Fuks, G.; Gurbatri, C.; Gopalakrishnan, V.; Kim, M.; Hurd, M. W.; Katz, M.; Fleming, J.; Maitra, A.; Smith, D. A.; Skalak, M.; Bu, J.; Michaud, M.; Trauger, S. A.; Barshack, I.; Golan, T.; Sandbank, J.; Flaherty, K. T.; Mandinova, A.; Garrett, W. S.; Thayer, S. P.; Ferrone, C. R.; Huttenhower, C.; Bhatia, S. N.; Gevers, D.; Wargo, J. A.; Golub, T. R.; Straussman, R. Potential Role of Intratumor Bacteria in Mediating Tumor Resistance to the Chemotherapeutic Drug Gemcitabine. *Science* **2017**, *357* (6356), 1156-1160.

(9) Zhou, S.; Gravekamp, C.; Bermudes, D.; Liu, K. Tumour-Targeting Bacteria Engineered to Fight Cancer. *Nat. Rev. Cancer* **2018**, *18* (12), 727-743.

(10) Galeano Niño, J. L.; Wu, H.; LaCourse, K. D.; Kempchinsky, A. G.; Baryiames, A.; Barber, B.; Futran, N.; Houlton, J.; Sather, C.; Sicinska, E.; Taylor, A.; Minot, S. S.; Johnston, C. D.; Bullman, S. Effect of the Intratumoral Microbiota on Spatial and Cellular Heterogeneity in Cancer. *Nature* **2022**, *611* (7937), 810-817.

(11) Iida, N.; Dzutsev, A.; Stewart, C. A.; Smith, L.; Bouladoux, N.; Weingarten, R. A.; Molina, D. A.; Salcedo, R.; Back, T.; Cramer, S.; Dai, R.-M.; Kiu, H.; Cardone, M.; Naik, S.; Patri, A. K.; Wang, E.; Marincola, F. M.; Frank, K. M.; Belkaid, Y.; Trinchieri, G.; Goldszmid, R. S. Commensal Bacteria Control Cancer Response to Therapy by Modulating the Tumor Microenvironment. *Science* **2013**, *342* (6161), 967-970.

(12) Darby, E. M.; Trampari, E.; Siasat, P.; Gaya, M. S.; Alav, I.; Webber, M. A.; Blair, J. M. A. Molecular Mechanisms of Antibiotic Resistance Revisited. *Nat. Rev. Microbiol.* **2023**, *21* (5), 280-295.

(13) Klugman, K. P.; Black, S. Impact of Existing Vaccines in Reducing Antibiotic Resistance: Primary and Secondary Effects. *Proc. Natl. Acad. Sci.* **2018**, *115* (51), 12896-12901.

(14) Jansen, K. U.; Knirsch, C.; Anderson, A. S. The Role of Vaccines in Preventing Bacterial Antimicrobial Resistance. *Nat. Med.* **2018**, *24* (1), 10-19.

(15) Kim, S. H.; Castro, F.; Paterson, Y.; Gravekamp, C. High Efficacy of a Listeria-Based Vaccine against Metastatic Breast Cancer Reveals a Dual Mode of Action. *Cancer Res.* **2009**, *69* (14), 5860-5866.

(16) Gao, W.; Fang, R. H.; Thamphiwatana, S.; Luk, B. T.; Li, J.; Angsantikul, P.; Zhang, Q.; Hu, C.-M. J.; Zhang, L. Modulating Antibacterial Immunity Via Bacterial Membrane-Coated Nanoparticles. *Nano Lett.* **2015**, *15* (2), 1403-1409.

(17) Zhou, J.; Kroll, A. V.; Holay, M.; Fang, R. H.; Zhang, L. Biomimetic Nanotechnology toward Personalized Vaccines. *Adv Mater.* **2020**, *32* (13), e1901255.

(18) Leventhal, D. S.; Sokolovska, A.; Li, N.; Plescia, C.; Kolodziej, S. A.; Gallant, C. W.; Christmas, R.; Gao, J.-R.; James, M. J.; Abin-Fuentes, A.; Momin, M.; Bergeron, C.; Fisher, A.; Miller, P. F.; West, K. A.; Lora, J. M. Immunotherapy with Engineered Bacteria by Targeting the Sting Pathway for Anti-Tumor Immunity. *Nat. Commun.* **2020**, *11* (1), 2739.

(19) Cabral, M. P.; García, P.; Beceiro, A.; Rumbo, C.; Pérez, A.; Moscoso, M.; Bou, G. Design of Live Attenuated Bacterial Vaccines Based on D-Glutamate Auxotrophy. *Nat. Commun.* **2017**, *8* (1), 15480.

(20) Ma, X.; Liang, X.; Li, Y.; Feng, Q.; Cheng, K.; Ma, N.; Zhu, F.; Guo, X.; Yue, Y.; Liu, G.; Zhang, T.; Liang, J.; Ren, L.; Zhao, X.; Nie, G. Author Correction: Modular-Designed Engineered Bacteria for Precision Tumor Immunotherapy Via Spatiotemporal Manipulation by Magnetic Field. *Nat. Commun.* **2023**, *14* (1), 4067.

(21) Pei, P.; Zhang, Y.; Jiang, Y.; Shen, W.; Chen, H.; Yang, S.; Zhang, Y.; Yi, X.; Yang, K. Pleiotropic Immunomodulatory Functions of Radioactive Inactivated Bacterial Vectors for Enhanced Cancer Radio-Immunotherapy. *ACS Nano* **2022**, *16* (7), 11325-11337.

(22) Lu, J.; Ding, J.; Chu, B.; Ji, C.; Zhang, Q.; Xu, Y.; Song, B.; Wang, H.; He, Y. Inactive Trojan Bacteria as Safe Drug Delivery Vehicles Crossing the Blood-Brain Barrier. *Nano Lett.* **2023**, *23* (10), 4326-4333.

(23) Zhang, F.; Lu, Y.-J.; Malley, R. Multiple Antigen-Presenting System (Maps) to Induce Comprehensive B- and T-Cell Immunity. *Proc. Natl. Acad. Sci.* **2013**, *110* (33), 13564-13569.

(24) Cheng, K.; Zhao, R.; Li, Y.; Qi, Y.; Wang, Y.; Zhang, Y.; Qin, H.; Qin, Y.; Chen, L.; Li, C.; Liang, J.; Li, Y.; Xu, J.; Han, X.; Anderson, G. J.; Shi, J.; Ren, L.; Zhao, X.; Nie, G. Bioengineered Bacteria-Derived Outer Membrane Vesicles as a Versatile Antigen Display Platform for Tumor Vaccination Via Plug-and-Display Technology. *Nat. Commun.* **2021**, *12* (1), 2041.

(25) Liu, G.; Ma, N.; Cheng, K.; Feng, Q.; Ma, X.; Yue, Y.; Li, Y.; Zhang, T.; Gao, X.; Liang, J.; Zhang, L.; Wang, X.; Ren, Z.; Fu, Y.-X.; Zhao, X.; Nie, G. Bacteria-Derived Nanovesicles Enhance Tumour Vaccination by Trained Immunity. *Nat. Nanotechnol.* **2023**.

(26) Toyofuku, M.; Nomura, N.; Eberl, L. Types and Origins of Bacterial Membrane Vesicles. *Nat. Rev. Microbiol.* **2019**, *17* (1), 13-24.

(27) Yang, G.; Xu, L.; Chao, Y.; Xu, J.; Sun, X.; Wu, Y.; Peng, R.; Liu, Z. Hollow Mno2 as a Tumor-Microenvironment-Responsive Biodegradable Nano-Platform for Combination Therapy Favoring Antitumor Immune Responses. *Nat. Commun.* **2017**, *8* (1), 902.

(28) Wang, C.; Xiao, Y.; Zhu, W.; Chu, J.; Xu, J.; Zhao, H.; Shen, F.; Peng, R.; Liu, Z. Photosensitizer-Modified Mno2 Nanoparticles to Enhance Photodynamic Treatment of Abscesses and Boost Immune Protection for Treated Mice. *Small* **2020**, *16* (28), 2000589.

(29) Qing, S.; Lyu, C.; Zhu, L.; Pan, C.; Wang, S.; Li, F.; Wang, J.; Yue, H.; Gao, X.; Jia, R.; Wei, W.; Ma, G. Biomineralized Bacterial Outer Membrane Vesicles Potentiate Safe and Efficient Tumor Microenvironment Reprogramming for Anticancer Therapy. *Adv Mater.* **2020**, *32* (47), e2002085.

(30) Palucka, K.; Banchereau, J. Cancer Immunotherapy Via Dendritic Cells. *Nat. Rev. Cancer* **2012**, *12* (4), 265-277.

(31) Wculek, S. K.; Cueto, F. J.; Mujal, A. M.; Melero, I.; Krummel, M. F.; Sancho, D. Dendritic Cells in Cancer Immunology and Immunotherapy. *Nat. Rev. Immunol.* **2020**, *20* (1), 7-24.

(32) Sabado, R. L.; Balan, S.; Bhardwaj, N. Dendritic Cell-Based Immunotherapy. *Cell Res.* **2017**, *27* (1), 74-95.

(33) Yan, J.; Wang, G.; Xie, L.; Tian, H.; Li, J.; Li, B.; Sang, W.; Li, W.; Zhang, Z.; Dai, Y. Engineering Radiosensitizer-Based Metal-Phenolic Networks Potentiate Sting Pathway Activation for Advanced Radiotherapy. *Adv. Mater.* **2022**, *34* (10), 2105783.

(34) Wang, C.; Guan, Y.; Lv, M.; Zhang, R.; Guo, Z.; Wei, X.; Du, X.; Yang, J.; Li, T.; Wan, Y.; Su, X.; Huang, X.; Jiang, Z. Manganese Increases the Sensitivity of the Cgas-Sting Pathway for Double-Stranded DNA and Is Required for the Host Defense against DNA Viruses. *Immunity* **2018**, *48* (4), 675-687.e677.

(35) Lv, M.; Chen, M.; Zhang, R.; Zhang, W.; Wang, C.; Zhang, Y.; Wei, X.; Guan, Y.; Liu, J.; Feng, K.; Jing, M.; Wang, X.; Liu, Y.-C.; Mei, Q.; Han, W.; Jiang, Z. Manganese Is Critical for Antitumor Immune Responses Via Cgas-Sting and Improves the Efficacy of Clinical Immunotherapy. *Cell Res.* **2020**, *30* (11), 966-979.

(36) Sun, X.; Zhang, Y.; Li, J.; Park, K. S.; Han, K.; Zhou, X.; Xu, Y.; Nam, J.; Xu, J.; Shi, X.; Wei, L.; Lei, Y. L.; Moon, J. J. Amplifying Sting Activation by Cyclic Dinucleotide–Manganese Particles for Local and Systemic Cancer Metalloimmunotherapy. *Nat. Nanotechnol.* **2021**, *16* (11), 1260-1270.

(37) Wang, M.; Rousseau, B.; Qiu, K.; Huang, G.; Zhang, Y.; Su, H.; Le Bihan-Benjamin, C.; Khati, I.; Artz, O.; Foote, M. B.; Cheng, Y.-Y.; Lee, K.-H.; Miao, M. Z.; Sun, Y.; Bousquet, P.-J.; Hilmi, M.; Dumas, E.; Hamy, A.-S.; Reyal, F.; Lin, L.; Armistead, P. M.; Song, W.; Vargason, A.; Arthur, J. C.; Liu, Y.; Guo, J.; Zhou, X.; Nguyen, J.; He, Y.; Ting, J. P. Y.; Anselmo, A. C.;

Huang, L. Killing Tumor-Associated Bacteria with a Liposomal Antibiotic Generates Neoantigens That Induce Anti-Tumor Immune Responses. *Nat. Biotechnol.* **2023**.